Materials Science and Engineering A 550 (2012) 103–111

Contents lists available at SciVerse ScienceDirect

Materials Science and Engineering A

journal homepage: www.elsevier.com/locate/msea

Microstructure evolution during cyclic tests on EUROFER 97 at room temperature. TEM observation and modelling

M.F. Giordana[a,*], P.-F. Giroux[b], I. Alvarez-Armas[a], M. Sauzay[b], A. Armas[a], T. Kruml[c]

[a] Instituto de Física Rosario, CONICET-UNR, Bv. 27 de Febrero 210 Bis, 2000 Rosario, Argentina
[b] Commissariat à l'Énergie Atomique, DEN/DANS/DMN/SRMA, 91191 Gif-sur-Yvette Cedex, France
[c] CEITEC IPM, Institute of Physics of Materials, Academy of Sciences of the Czech Republic, Žižkova 22, Brno, 616 62, Czech Republic

ARTICLE INFO

Article history:
Received 15 December 2011
Received in revised form 27 March 2012
Accepted 5 April 2012
Available online 17 April 2012

Keywords:
Martensitic steels
Softening behaviour
Microstructural evolution
Polycrystalline modelling

ABSTRACT

The 9% Cr quenched and tempered reduced-activation ferritic/martensitic steel EUROFER 97 is one of the candidates for structural components of fusion reactors. Isothermal, plastic strain-controlled, low-cycle fatigue tests are performed. Tested at room temperature, this steel suffers a cyclic softening effect linked to microstructural changes observed by transmission electron microscopy, such as the decrease of dislocation density inside subgrains or the growth of subgrain size. From the assumed mechanisms of softening a simple mean-field model based on crystalline plasticity is proposed to predict these microstructure evolutions during cycling and monotonic deformation.

1. Introduction

High-chromium ferritic/martensitic steels have been extensively used because of their economical combination of good mechanical and corrosion resistance at elevated temperatures [1]. These properties, in addition to their ability to resist the effects of high doses of irradiation, focused the interest on these alloys for first-wall and blanket structure components of fusion reactors. The pulsed mode operation of fusion devices leads to cyclic loading at high temperatures of the structural materials during operation. This fatigue process may be sufficiently severe to cause damage to the material.

Although pronounced ageing does not produce marked changes in the tempered martensite lath structure of the steels [2], it is evident from previous results [3] that continuous cycling produces changes in the microstructure and a marked cyclic softening. This effect could become a significant engineering problem affecting creep after precycling, swelling and segregation phenomena during irradiation. Although the origin of the effect and the kinetics of the softening behaviour are not completely understood, it is mainly attributed to two different microstructural evolutions: the free dislocation density decreases, and also some Low-Angle Boundaries (LABs) disappear, during cycling, which explains subgrain size growth [4]. However, blocks do not suffer any structural change during cycling [5,6]. Several authors have studied the tempered martensite lath structure in different steel types and have observed the same microstructural evolution; i.e. Kunz and Lukás [7], and Fournier et al. [8,9] worked with P91 steel, Ennis et al. [10] and Giroux et al. [11,12] with P92, Armas et al. with MANET II and F82H [3,13] and Marmy and Kruml [14,15] with EUROFER 97. A comparison of the cyclic behaviour between various 9–12%Cr steels is presented by Fournier et al. [16]. In any way, the authors show that the cyclic softening effect is correlated with the decrease of dislocation density and to the subgrain growth. The softening seems to be intrinsic to the lack of stability of the tempered martensitic structure whatever the chemical composition and heat treatment.The detailed analysis of the microstructure evolution, the observation of the evolving surface and the measurement of the mechanical properties leads to a better understanding of the crack initiation and growth [17]. During the first part of the fatigue life dislocations evolve to a stabilized characteristic internal structures. This is followed by the localization of the cyclic plastic strain into bands; Fournier et al. show short slip bands in the surface of P91 steel [18]. Kruml and Polák [19] show that first fatigue cracks always nucleate along particular dislocation structures; no nucleation event is found to be related to precipitates, inclusions or other microstructural defects. Therein lies the importance of the very detailed study of dislocation structure during cyclic loadings for better understanding the damage produced by fatigue. Furthermore, this analysis is the starting point for the modelling of fracture of the surface oxide layer due to the alloy deformation [20].

* Corresponding author. Tel.: +54 341 4808545; fax: +54 341 4853200.
E-mail address: giordana@ifir-conicet.gov.ar (M.F. Giordana).

0921-5093/$ – see front matter © 2012 Elsevier B.V. All rights reserved.
http://dx.doi.org/10.1016/j.msea.2012.04.038

Table 1
Chemical composition of EUROFER 97 steel (wt.%).

C	Cr	Ni	Mo	V	Nb	Si	Mn	Ta	B	W	N	Fe
0.12	8.93	0.022	0.0015	0.2	0.0001	0.06	0.47	0.14	<0.001	1.07	0.018	Bal.

In addition, Fournier et al. [16], during their study of creep, fatigue and interactions, present the strong effect of precycling at very low amplitude on further creep. This problem is being extensively studied [21,22], finding that the coarsening of the dislocation structure due to cyclic deformation induces drastic reduction of creep resistance. Therefore, consequences of cyclic loading, specially subgrain growth, are not only essential for studying fracture, but also they are important for predicting lifetime during creep tests.

Recently, a micromechanical model has been proposed for predicting both the microstructure evolution and the macroscopic softening of a rather similar material [11]. This model based on the self-consistent Kröner homogenization model [23] is suitable for elastic–plastic constitutive laws. The self-consistent scheme is referred to the problem of an inclusion embedded in an infinite matrix. Each martensite block of the polycrystal is successively regarded as an inclusion within the matrix made of all other blocks, the behaviour of the polycrystal is then calculated by an average process over all blocks. Based on the identified mechanisms of microstructure evolution determined by TEM observations, a mean field polycrystalline model is proposed to predict the microstructure evolution. Particularly, two different softening mechanisms are taken into account: the decrease of the dislocation density inside the subgrains and subgrain size growth. The subgrain growth is mostly due to the disappearance of LAB dislocations. Using physical parameters, mainly determined by microstructural observations, modelling allows the prediction of the dislocation structure evolution which is compared to TEM observations.

2. Material and experimental procedures

Plastic strain-controlled, low-cycle fatigue (LCF) tests are conducted on EUROFER 97 using an electromechanical INSTRON testing machine. Cylindrical specimens with two different geometries are manufactured, type I of 8.8 mm diameter and 21 mm in gauge length and type II of 2.7 mm diameter and 6 mm in gauge length. Tests are carried out in air at room temperature (RT) using plastic strain ranges $\Delta\varepsilon_p = 0.2$, 0.3, 0.6% for samples of type I and using total strain range $\Delta\varepsilon_t = 0.8\%$ for type II, the total strain rate, in both cases, is $\dot{\varepsilon} = 2 \times 10^{-3}\,s^{-1}$. The manuscript is based on the tests performed with tests type I specimens. The results of type II specimens are performed by P. Marmy at Centre de Recherches en Physique des Plasmas, École Polytechnique Fédérale de Lausanne, Switzerland, and are used at the end of the article for comparison.

The chemical composition of the material in weight percent is given in Table 1. The thermal treatment consists of an austenitizing at 980 °C for 30 min followed by air cooling and a final tempering at 760 °C for 90 min followed also by air cooling. The resulting microstructure is tempered martensite with a crystallographic structure very close to the body centred cubic crystal (BCC) due to carbide precipitation.

Specimens are examined by transmission electron microscopy (TEM) using two different microscopes, Philips EM 300 operating at 100 kV, for general structure, and Philips CM 200 operating at 200 kV, for detailed microstructure studies. Several scales are involved in the EUROFER 97 structure [24]: prior austenitic grains, packet of blocks, block of laths, martensitic laths and subgrains, Fig. 1(b). Electron back scattered diffraction (EBSD) measurements show that the misorientation angles between laths or subgrains from the same block are lower than 5°. Furthermore, as can be seen in Fig. 1(a), the structure inside each block is composed mainly of many submicrometric equiaxed subgrains; the dislocation density inside the subgrains is very high. The average block size measured by EBSD is 3.1 μm.

The subgrain size is measured from TEM bright field micrographs, by determining the area of each micrograph and counting the number of subgrains within it, assuming the shapes of the subgrains as circular disks. The experimental error in the measurement of the subgrain size is estimated by calculating the standard deviation (σ) of the subgrain measures obtained from several micrographs (about 10).

In order to determine the average value of the dislocation density inside subgrains, or free dislocation density, a mean linear intercept method is adopted [26]. The free dislocation density value is determined, in the as-received material as well as in the different tested samples, using the following equation,

$$\rho = 2\frac{\sum_i n_i}{t\sum_i l_i} \tag{1}$$

With t the local thickness of the thin foil, l_i the length of the plotted segment i and n_i the number of intersections between the segment i and dislocations. The local thickness of the thin foils is assumed to be 0.1 μm and the measurement error is estimated to be 25% [27]. This assumption was based on the idea that in thinner foils, dislocations were not easily observed because of the bent of the sample,

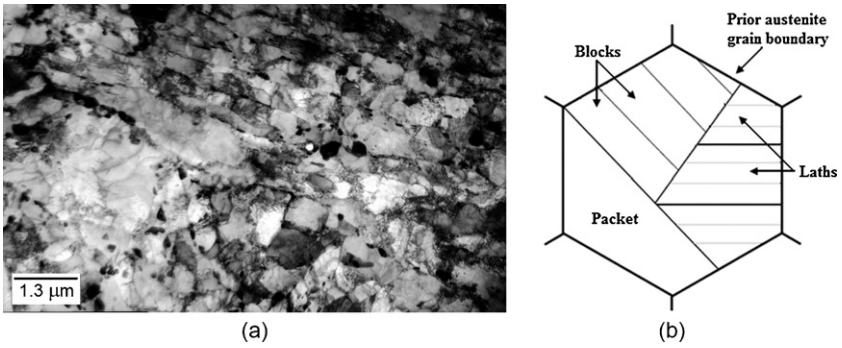

Fig. 1. (a) Tempered martensite structure of as-received samples after normalization and tempering treatment and (b) schematic microstructure [25].

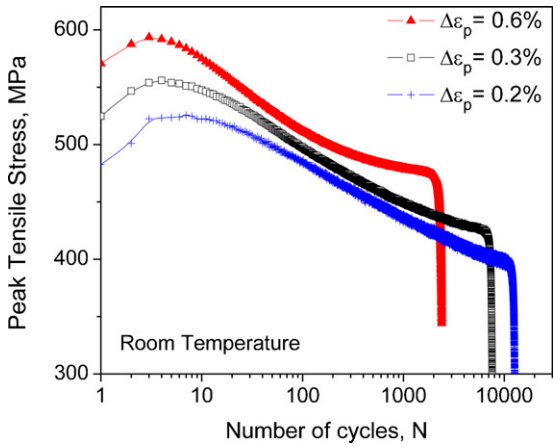

Fig. 2. Cyclic softening curves obtained at RT using three different plastic strain ranges.

and in thicker foils the transparency is not enough, even for a TEM operating at 200 kV [28]. The evaluation of the experimental errors is carried out according to Taylor [29]. More than 20 measures of the density are carried out for each test condition. Therefore, the error for the measured free dislocation density is estimated by calculating the mean standard deviation ($\sigma N^{-1/2}$). An extra dispersion of 10% in order to take into account the error that was introduced throughout the estimation of the thickness of the sample.

3. Experimental results

3.1. Mechanical tests results

Fig. 2 shows the cyclic softening behaviour commonly observed in EUROFER 97 fatigued at room temperature using three different plastic strain ranges 0.2%, 0.3% and 0.6%. As can be seen in Fig. 2 the peak tensile stress of each hysteresis loop shows a continuous softening up to fracture, which is much more pronounced at the beginning of the fatigue life. At the very beginning, a very short hardening behaviour can be observed.

The maximum peak tensile stress for each curve is observed during the first cycles. After this very short consolidation phase, the cyclic stress amplitude decreases rapidly. All the curves present quite similar behaviours, that is, a transitional stage corresponding to the first part of the fatigue life followed by an almost linear second stage (in a semi-log scale). The first stage depends on the plastic strain range being shorter for the higher plastic strain range. It should be noticed that no saturation of the softening is observed in agreement with long term cyclic test results provided the plastic strain range is not negligible. These ones concern either low amplitude test in air [16], in-vacuum test [30] or in-sodium tests [31].

3.2. TEM observations

Fig. 3(a–c) shows the characteristic subgrain structures for samples fatigued up to fracture at room temperature with plastic strain ranges of 0.2%, 0.3% and 0.6%, respectively. Cycling at RT induces two visible microstructural evolutions [4]. First and the most evident, the free dislocation density decreases during cycling (compare Fig. 1 with Fig. 3). Some dislocations can be observed mainly in small subgrains, suspected not to be deformed plastically, or pinned by precipitates. Second, some LABs disappear during cycling, which explains subgrain size growth.

Additional information about the relationship between the cyclic softening and the microstructure evolution, in the same or similar materials at room temperature, is possible to be found in the literature [14,32]. These evolutions are in fact observed in all tempered martensite ferritic steels, which produces cyclic softening, particularly at high temperature.

4. Physically based modelling

4.1. Polycrystalline homogenization

A simple mean-field modelling based on crystalline elasto-plasticity is applied in order to predict the polycrystalline cyclic stress–strain curves (CSSCs). The crystallographic structure is body centred cubic. Therefore, two families of slip systems are considered, {1 1 0} and {1 1 2} slip planes and <1 1 1> slip directions, which all together represent 24 slip systems [33]. Simulations are carried out considering a polycrystal composed of 100 crystals, or martensite blocks, with randomly distributed orientations. Based on the Kröner model, the localization rule is given by the interaction law as follows,

$$\underline{\underline{\sigma}} = \underline{\underline{\Sigma}} + 2\mu(1-\beta)(\underline{\underline{E}}^{p} - \underline{\underline{\varepsilon}}^{p}) \text{ with } \beta = \frac{2(4-5\nu)}{15(1-\nu)} \quad (2)$$

Here, σ and Σ are respectively the local (i.e. in the considered block) and macroscopic stress tensors; and ε^p and E^p are the local and macroscopic plastic strain tensors; ν is the Poisson's ratio equal to 0.3, and final, the shear modulus, measured experimentally, is $\mu = 82$ GPa. Blocks are assumed to obey isotropic elasticity. The Kröner localization rule uses the macroscopic elastic moduli for describing the block/matrix interaction (thermo-elasticity framework). This model gives reasonable results for low plastic strain, and the macroscopic stress is overestimated by less than 15% for macroscopic plastic strain range of 0.4% [34]. Kröner model is also relevant for predicting the mechanical behaviour at RT, for which no influence of the strain rate is observed. A similar model has been used by Giroux et al. [11], for predicting cyclic softening but at high temperature. Therefore, some extra considerations should be taken into account.

For tempered ferritic/martensitic steels, the block of laths is observed to be the smallest imbricated microstructural scale that is stable during cycling. Therefore, modelling is carried out at block scale. Each block of laths is considered as a phase with an almost homogeneous crystallographic orientation. The model predicts the mechanical behaviour of a block embedded in the matrix isotropic composed of a large number of other blocks. Due to the fact that during cycling almost all microstructural changes take place inside blocks, homogenization modelling starts at the scale of blocks using block average dislocation density and subgrain size; moreover, mean block size is the upper limit for subgrain size growth.

4.2. Crystalline constitutive laws at block scale

Considering one block and the slip system i, the shear stress τ^i is expressed in function of the projection of the local stress tensor σ on the i^{th} slip system in the following way,

$$\tau^i = \sigma : (m^i \otimes n^i) \quad (3)$$

With m^i is the slip direction and n^i is the normal to the slip plane. The critical shear stress τ_c, corresponding to the sum of the critical shear stress on each of the 24 slip systems and required to activate the plastic slip, is supposed to be the same for all slip systems. The isotropic stress law is expressed as:

$$\tau_c = \tau_0 + \alpha\mu b\sqrt{\rho_e + \rho_s} \quad (4)$$

Where α is a constant equal to 0.3 for BCC crystals [35], ρ_e and ρ_s are the free dislocation densities for edge and screw dislocations, respectively, and b is the Burger's vector module. In pure Iron, τ_0

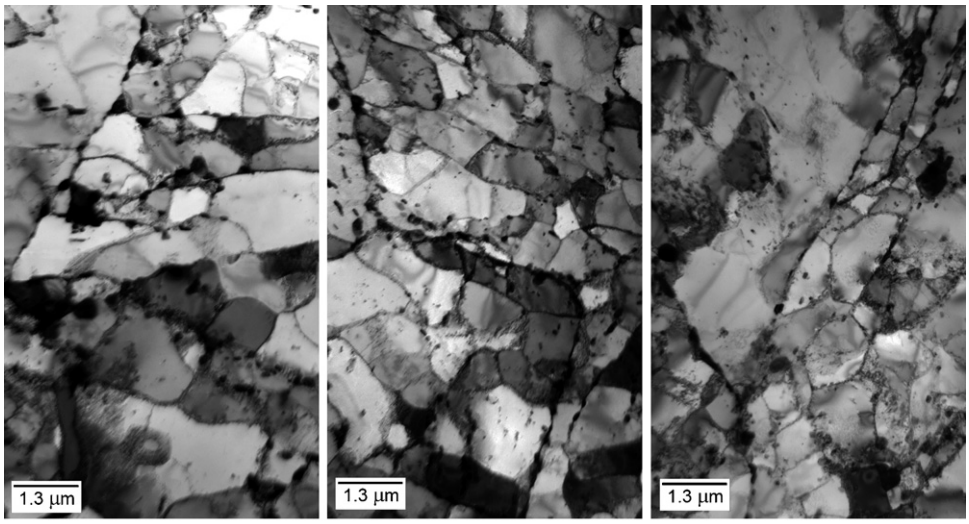

Fig. 3. Subgrain structure for samples fatigued up to rupture at RT with $\Delta\varepsilon = 0.2\%$ (a), 0.3% (c) and 0.6% (c).

Table 2
Parameters and their value required for modelling.

T	293 K		b	2.54×10^{-10} m	
k	1.38×10^{-23} J K^{-1}		y_e	2 nm	[33]
ν_0	10^{13} s^{-1}	[40]	y_s	50 nm	[33]
μ	82 GPa		ρ_0	2.4×10^{14} m^{-2}	TEM measurements
ν	0.3		θ_0	2.5°	EBSD measurements
α	0.3	[31]	d_0	0.7 μm	TEM measurements
Adjustable parameter:			τ_0	100 MPa	

is linked to the energy necessary for dislocations to move to the next Peierls' valley [36] and to the solid solution effect. The Peierls thermally-activated process mainly depends on temperature and on viscoplastic strain rate. Nevertheless, even when the Peierls stress is low at RT [36], a negligible value cannot be attributed to τ_0 because of the solid solution effect, see Table 2.

4.2.1. LAB misorientation and subgrain size growth

During cycling, the dislocation density along the LABs is assumed to decrease only because of interactions with the free dislocations (knitting reactions) [37]. For a given slip system i and a given dislocation type (edge or screw), the evolution of average misorientation is expressed as:

$$\dot{\theta}^i_e = -\theta^i_e \frac{y_e}{b}\dot{\gamma}^i_{e,cum} \quad \text{and} \quad \dot{\theta}^i_s = -\theta^i_s \frac{y_s}{b}\sum_{j\in\Omega}\dot{\gamma}^j_{s,cum} \tag{5}$$

y_e (y_s) is the athermal edge (screw) annihilation distance, equal to about $6b$ (resp. $200b$) for copper at room temperature [38]. The values of the annihilation distances depend on crystal material and temperature. Concerning these parameters, a limited number of studies are available in literature and no measurements have been performed on 9% Cr tempered martensitic steels. Consequently, and due to the fact that, even at RT, the Peierls effect is low in the material under study [36], the slip mechanisms of dislocations in BCC structure are considered to be similar to those in face centred cubic structure [37]. Then, using y_e and y_s corresponding to copper may be suitable. Subgrain boundaries are here considered to be composed of either edge or screw dislocation types in equal quantities. Their corresponding misorientations (θ^i_e and θ^i_s respectively) are weighted values of the misorientation of each subgrain boundary type.

The decrease in average subboundary misorientation angle in the material during deformation is predicted by modelling proposed in [39]. Following the dislocation dynamics computations of Holec and Dlouhy [40], when the misorientation angle is lower than a critical value, interaction forces between LAB dislocations and the $M_{23}C_6$ precipitates are too weak to preserve LAB stability under stress loading. This leads to the disappearance of the low-angle boundary. Taking into account the LAB precipitate feature of tempered martensitic/ferritic steels, the critical misorientation angle is about 0.3° [40]. Based on the ratio of vanished LABs [12], an estimation of subgrain growth is carried out. Subgrains are modelled as cubes with edge length ϕ_0 and LABs correspond to the faces of these cubes. In a given unit volume homogeneously deformed in tension, the initial surface S_0 per unit volume made of low-angle boundaries is computed by:

$$S_0 = \frac{1}{\phi_0^3}\phi_0^2\frac{6}{2} = \frac{3}{\phi_0} \tag{6}$$

The first term $1/\phi_0^3$ corresponds to the number of cubes in the considered unit volume, ϕ_0^2 is the surface of one low-angle boundary and 6/2 is the number of faces per cube (two neighbour cubes share the same face). The vanishing of a proportion κ of LABs during deformation is supposed to be quite isotropic. All subgrains are assumed to remain cubic with a uniform increase in edge length ϕ. Then, annihilation of boundaries leads to a decrease in S_0. In the same way as Eq. (6), the surface per unit volume filled with LABs, S, can be computed as a function of the edge length ϕ of the cube after deformation:

$$S = \frac{3}{\phi} \tag{7}$$

Then, the relationship between S_0 and S is:

$$S = (1-\kappa)S_0 \tag{8}$$

4.2.2. Back stress–Bowing-out of a dislocation

In the as-received material, many mobile dislocations seem to be straight lines, pinned at subgrain boundaries [41,42]. Under stress, the resolved shear stress applied on a given slip system i induces the bowing-out of these dislocations [43]. Fig. 4(a) shows a schematic representation. During one cycle, the evolution of the local back stress on each slip system is computed based on a simple tension line model in dislocation microstructures [44,45].

Based on Fig. 4(a) it is possible to deduce a relationship between the plastic slip, γ, and the radius of curvature of the dislocation,

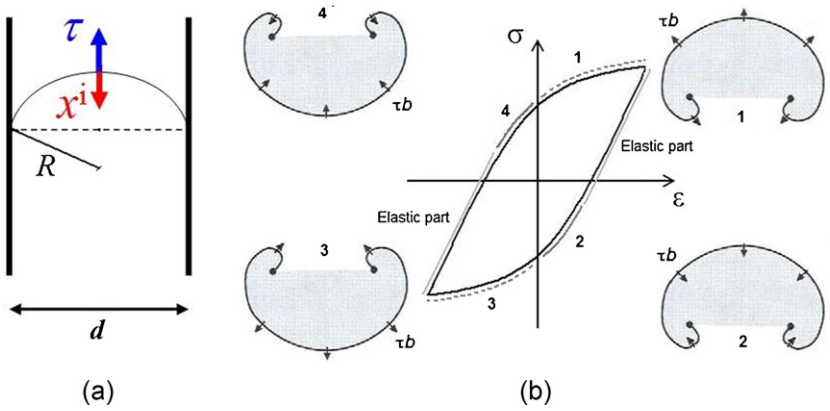

Fig. 4. (a) Scheme of a mobile dislocation pinned up at subgrain boundaries and bowing-out under shear stress τ; (b) scheme of a Frank-Read source on an arbitrarily selected slip system during cycling.

R, in the following way. During the bowing-out, the Orowan formula permits to express the plastic slip as a function of the mobile dislocation density $\rho_e^i + \rho_s^i$ on the slip system i:

$$\gamma^i = \left(\rho_e^i + \rho_s^i\right) lb \tag{9}$$

Where b is the Burger's vector and l is defined as the area swept by the dislocation divided by the subgrain size (d). The computation of this length in Appendix A allows us to deduce the following relationship:

$$\gamma^i = \frac{\left(\rho_e^i + \rho_s^i\right) b}{d}\left[R^2 arctg\left(4\frac{R^2}{d^2} - 1\right)^{-1/2} - \frac{d}{4}\left(4R^2 - d^2\right)^{1/2}\right] \tag{10}$$

In this equation R is the curvature radius of the dislocation depending on the local shear stress.

Each element of the curved free dislocation is under equilibrium between the force resulting from the shear stress $F^i = \tau^i b$ and the tension line T [46], which is different for edge and screw dislocations [44]. Dupuy and Fivel [47] has shown that the critical shear stress required to complete the bowing-out of a dislocation segment of a Frank-Read source weakly varies between a initially pure edge segment and a pure screw one. Therefore, for the sake of simplicity an average value of the tension line for edge and screw is used ($T \approx 1/2\mu b^2$).

$$R = \frac{T}{F^i} = \frac{\mu b}{2\tau^i} \tag{11}$$

The local back stress x^i acting on the slip system i is defined as the stress induced by the tension line. Its value is thus given by:

$$x^i = \frac{\mu b}{2R} \tag{12}$$

Relating the plastic slip and the back stress through the radius of curvature (cf. Appendix B), the following equation is obtained, presented here in the differential form:

$$\dot{x}^i = \frac{2d\left(x^i\right)^3\left(\dot{\gamma}_e^i + \dot{\gamma}_s^i\right)}{\left(\rho_e^i + \rho_s^i\right) b^3\mu^2} \times \left\{\frac{1}{2}\left[\frac{\mu^2 b^2}{\left(x^i\right)^2 d^2} - 1\right]^{-1/2} - \arctan\left[\frac{\mu^2 b^2}{\left(x^i\right)^2 d^2} - 1\right]^{-1/2}\right\}^{-1} \tag{13}$$

4.2.3. Dislocation density evolution

For a given slip system i, the difference in the behaviour of edge and screw dislocations leads us to express the variation of density of free edge and screw dislocations separately, as a function of the plastic slip (γ). First, the rate of production of dislocations during cycling is determined, and then the rate of annihilation of dislocations for a plastic slip rate $\dot{\gamma}$. To study the production of dislocations, the Frank-Read source activation during four different steps is considered. The hysteresis loop presented in Fig. 4(b) is divided into six parts, two of them correspond to the elastic parts, and no dislocation glide occurs during these periods. Parts 1 and 4 are in tension, and 2 and 3 are in compression. For the sake of simplicity, any microplasticity mechanism is neglected during macroscopic elastic loadings and unloadings.

During part 1, the usual activation of the Frank-Read source takes place and the rate of production of edge dislocations could be written as follows [38]:

$$\dot{\rho}_e^{i+} = \frac{2}{bd}\dot{\gamma}_s^i \tag{14}$$

The hypothesis which consists in describing the dislocations as pure edge or pure screw leads us to model the loops as squares or rectangles. In this case, when the screw dislocations glide ($\dot{\gamma}_s^i$), the length of the edge dislocations is increased ($\dot{\rho}_e^{i+}$). During part 2, it is considered that the dislocations come back to the source, annihilating one another. The sign of the applied shear stress on a given slip system changes depending on time (tension or compression parts). It induces a modification of the sign of glide and so, a variation of the terms of production of dislocations. Parts 3 and 4 are described in the same way as parts 1 and 2, even when the bowing-out of the dislocation occurs in the opposite direction.

During plastic slip on an activated slip system i, two parallel free dislocations can annihilate together if their Burger's vectors are opposite and if their inter-spacing distance is lower than the critical spontaneous annihilation distance. The rate of annihilation of parallel and opposite dislocations, for the four different parts, is expressed by Essmann and Mughrabi [38] in the following way,

$$\dot{\rho}_e^{i-} = -2\frac{y_e}{b}\rho_e^i\dot{\gamma}_{e,cum}^i \tag{15}$$

Then, for the total evolution of edge dislocation density it is obtained,

$$\dot{\rho}_e^i = \dot{\rho}_e^{i+} + \dot{\rho}_e^{i-} = \frac{2}{bd}\dot{\gamma}_s^i - 2\frac{y_e}{b}\rho_e^i\dot{\gamma}_{e,cum}^i \tag{16}$$

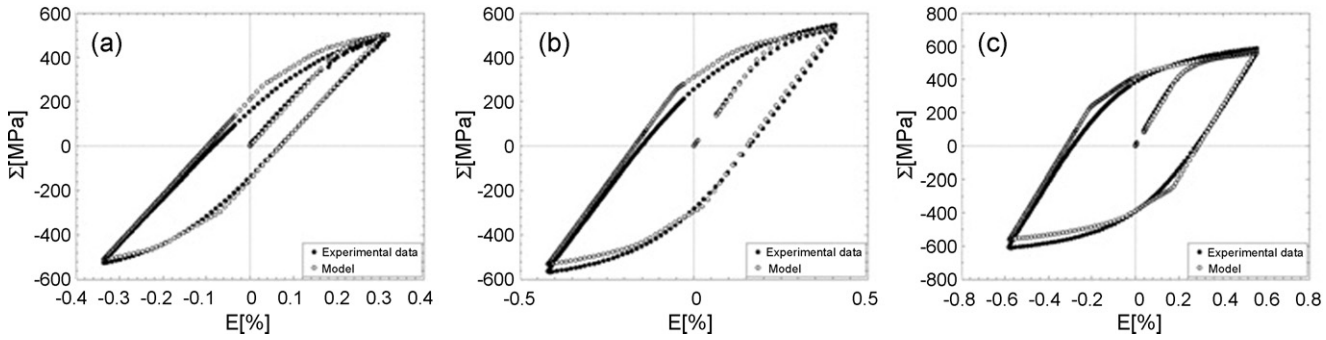

Fig. 5. Comparison between experiments and simulation: first stress–strain loops using plastic strain ranger of (a) 0.2%; (b) 0.3% and (c) 0.6%.

For screw dislocations, the formula is more complex because of the number of slip planes that have to be considered for a given Burger's vector:

$$\dot{\rho}_s^i = \dot{\rho}_s^{i+} + \dot{\rho}_s^{i-} = \frac{2}{bd}\dot{\gamma}_e^i - \frac{y_s}{b}\left(\dot{\gamma}_{s,cum}^i \sum_{j\in\Omega}\rho_s^j + \rho_s^i \sum_{j\in\Omega}\dot{\gamma}_{s,cum}^j\right) \quad (17)$$

Dislocation annihilation in a given slip system *i* leads to the vanishing of two parallel and opposite dislocations, which is modelled by the factor 2 in Eq. (15). For screw dislocations in BCC crystals, the Burger's vector and slip direction are parallel. Consequently, from a computation point of view, a screw dislocation belongs to six slip systems. This set of 6 slip planes is designed by Ω. This method is characterized by a careful treatment of the annihilation of screw dislocations, more evolved than in previous developed model [9].

One of the characteristics of the previous equations is the coupling edge glide and screw production and vice versa, which is only rarely taken into account.

4.3. Parameter values

The crystal plasticity constitutive laws are based on: the Schmid criterion, Eq. (3), the Taylor equation, Eq. (4), and the kinematic stress hardening evolution law, Eq. (13). Therefore, block behaviour could be considered as elastic–plastic in agreement with test results showing a negligible strain rate effect at RT. The identification of the parameters is carried out in three different steps. In the first one, the material parameters (μ, ν, ν_0, α, k, b, y_e, y_s) have been estimated from literature or from simplifying assumptions. In the second step, the initial dislocation density and sub grain size (ρ_0, d_0) are estimated from our extensive experimental TEM measurements. As well, the mean initial misorientation value inside blocks (θ_0) is measured thanks to electron back scattered diffraction made at Commissariat à l'Énergie Atomique, SRMA, CEA France. Finally, in the last step, the τ_0 value (Eq. (4)) is adjusted. Instead of taking τ_0 equal to zero as it was done by Giroux at 550 °C [11], this parameter has been adjusted in order to reproduce, as best as possible, the first quarter of the first cycle at RT. At room temperature, the solid solution and precipitate effects are indeed no longer negligible. The set of parameters and their values are summarized in Table 2.

5. Results and discussion

5.1. First loops and monotonic behaviour

The optimization of the τ_0 parameter is carried out using only the first loop at a plastic strain range of 0.6%. Thus, in order to validate the proposed modelling, tests using plastic strain ranges 0.2% and 0.3% are simulated and compared to experimental data. Fig. 5 shows the results of modelling for the first cycles. Although only one parameter has been adjusted (τ_0), predictions are in good agreement with experimental stress–strain curves.

In addition, a tensile test is carried out up to 8% of deformation, obtaining a predicted curve, which fits well with the experimental one. Furthermore, it is known from previous TEM observations results [48] that under monotonic loading at RT, EUROFER 97 does not present evolution of the microstructure up to 1.5% of deformation. The predicted mean subgrain size, in agreement with experiments, is rather constant up to 2%. The results for the evolution of free dislocation density are also acceptable, but it depends slightly on the percentage of initial screw dislocation density as well as on the annihilation distances. Higher cumulated plasticity is needed for predicting non negligible microstructure evolutions.

5.2. Stability with respect to parameter values

Using a physically-based modelling allows us to avoid using more than one or two adjusted parameters. However, not all of the other parameter values are perfectly known. In some cases, only the range to which the parameter belongs is known. Consequently, it is critical that a slight change in the parameter values does not lead to large differences in predicted results. Therefore, a study of the stability of the predictions with respect to some other parameter values is made. Computations are carried out using different values, following the literature review, for the following parameters: $y_e \in (1\,\text{nm} - 5\,\text{nm})$, $y_s \in (25\,\text{nm} - 100\,\text{nm})$ [39], $\tau_0 \in (0\,\text{MPa} - 150\,\text{MPa})$, $\theta_0 \in (2^\circ - 3^\circ)$ (measurement error: $\pm 0.5^\circ$) and $\rho_s \in (\rho_t/2 = 1.2 \times 10^{14}\,\text{m}^{-2} - \rho_t = 2.4 \times 10^{14}\,\text{m}^{-2})$ [49]. TEM observations [49] show that most of the free dislocations seem to be close to screw ones. The results of this study show that the predictions are rather stable with respect to these variations. As an example, Fig. 6 shows three different predictions for the evolution

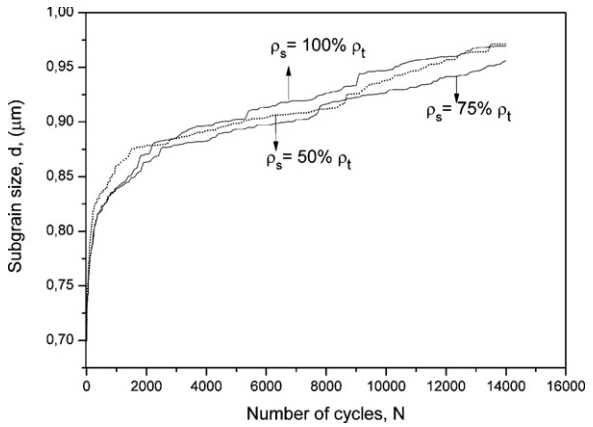

Fig. 6. Stability of the prediction of subgrain growth with respect to the partition between edge and screw dislocations.

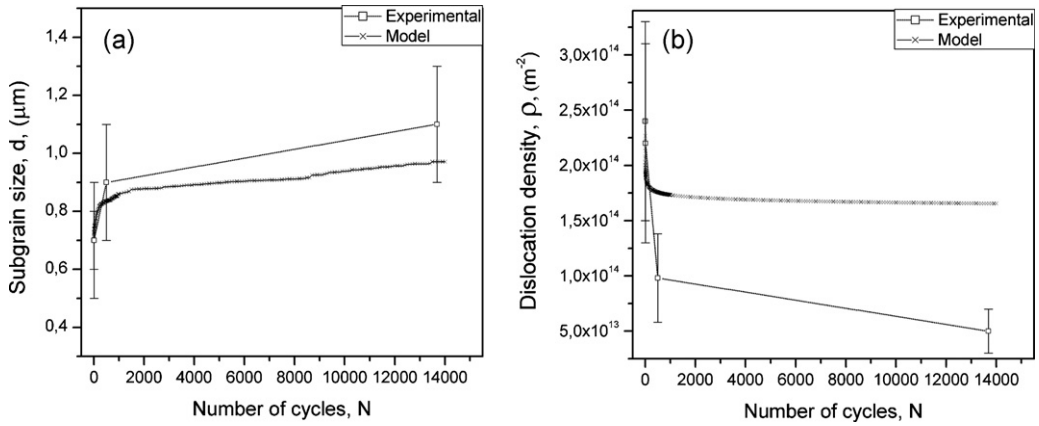

Fig. 7. Predicted and experimental microstructural evolutions: (a) subgrain size and (b) dislocation density.

Table 3
Microstructural evolution predicted by modelling for two different tests, one up to 500 cycles and the other one up to rupture, and comparison with experimental values.

Number of cycles	0	500	14000
$\Delta\varepsilon_p$ (%)	0.2	0.2	0.2
d_{exp} (μm)	0.7 ± 0.1	0.9 ± 0.2	1.1 ± 0.2
d_{pred} (μm)	0.7	0.8	0.9
ρ_{exp} (10^{14} m^{-2})	2.4 ± 0.9	1.0 ± 0.4	0.5 ± 0.2
ρ_{pred} (10^{14} m^{-2})	2.4	1.7	1.6

of the mean subgrain size. In the first one it is considered that the free dislocation population is equally divided into edge and screw dislocations, in the second case the screw dislocation density represents the 75% of the total free dislocation density, and the last one takes into account only screw dislocations following some TEM observations [49]. As it is showed in Fig. 6, the prediction of the subgrain size is stable with respect to the variation in free dislocation density partitioning. Increasing screw dislocation density by a factor 2 leads to a variation in the final subgrain size lower than 1.5%. Similar results are obtained with all the other parameters.

5.3. Microstructure evolutions

The fatigue life of the material is modelled, taking into account both the back stress and dislocation density evolution laws proposed in Section 4. Results are represented in Table 3. Two different cases are taken into account, one cycled up to $N = 500$ and the other one cycled up to $N = 14000$, this last one corresponds to the sample fatigued up to rupture. Predictions for the mean subgrain size underestimate slightly the value obtained experimentally. For $N = 500$, the subgrain size is underestimated in approximately 10%, and for rupture test, the underestimation is near 20%. Nevertheless, following the observations of samples type II, Table 4, no substantial subgrain size growth is visible [14], therefore, there is an overestimation of the results. Thus, modelling gives reasonable predictions for the evolution of the subgrain size during cycling. That is not the case for dislocation density evolution; the values obtained experimentally are far away from the ones predicted. So, modelling has to be improved to describe more properly the decrement of free dislocation density. Nevertheless, for P91 steel Kunz and Lukás [50] do not observe strong dislocation density evolutions at RT. And the predicted evolutions once more underestimate the evolutions that we observed but overestimate the ones observed by other authors.

Fig. 7 shows the comparison between the predicted and experimental microstructural evolutions. In the case of subgrain size, even if the final value is slightly underestimated, the evolution during cycling is quite well reproduced by modelling. For dislocation density evolution, the results clearly show an overestimation of the mean value obtained for EUROFER 97. Nevertheless, the striking feature of Fig. 7 is that experimental and predicted evolutions are qualitatively similar with a quick decrease at the beginning and then continuous but lower evolution. It is important to notice that, the decrease in dislocation density during cycling, is significant when considering our measured values, which are corroborated qualitatively with observations of sample type II. However, in similar materials, such as P91, this evolution is not as marked as the one observed in EUROFER 97. Further work is required for taking into account the initial microstructure data of each material which are required for predicting microstructure evolutions.

Work is in progress in order to use the Hill–Hutchinson mean-field homogenization modelling [51,52] to obtain more accurate predictions. Rachdi and Sauzay [34] used this modelling for predicting, and the finite elements full-field computation results show that the HH modelling overestimates the macroscopic stress by less than 6%, even for macroscopic plastic strain amplitude of 1%. In any case, no significant difference is expected at low plastic strain. Other main implement will concern fracture modelling, improving predictions of the fatigue/creep lifetimes, predictions of the plastic behaviour for studying oxide fracture and crack-resharpening. The prediction of creep behaviour of precycled specimen may be carried out using similar modelling and the results of previous simulations as input data. In addition, some other aspects related to dislocation movements, such as climb, are going to be taken into account in order to improve the prediction for high temperature tests. Furthermore, a localization law adapted from the approach of Molinari et al. [53] will be implemented in the model in order to better approximate the viscoplastic behaviour of these steels.

Table 4
Subgrain size predicted by modelling and comparison with the values measured using the specimens tested by Marmy and Kruml using a total strain range 0.8% [14].

Number of cycles	0	6100
$\Delta\varepsilon_t$ (%)	0.8	0.8
d_{exp} (μm)	0.7	0.9
d_{pred} (μm)	0.7	1.0

6. Conclusions

Low-cycle fatigue tests using three different plastic strain ranges (0.2%, 0.3% and 0.6%) are carried out at room temperature on EUROFER 97 steel. Experimental results show a pronounced cyclic softening, which is accompanied by microstructural changes, such as the decrease of the dislocation density inside blocks and

the disappearance of low-angle boundaries. The major effect produced by cycling at room temperature is a "cleaning out" of the dislocations inside the subgrains.

Simulations are carried out considering that the crystallographic structure of the material is body-centred cubic, which leads to consider 24 slip systems. In addition, it is supposed that the free dislocation density is equally divided into edge and screw types; and it is taken into account that the polycrystal is composed of 100 crystals, or martensite blocks, with randomly distributed orientations. Based on the Kröner model, the homogenization modelling gives reasonable predictions for tensile loading, as well as for the first cycles, for EUROFER 97 at 20 °C. In agreements with tensile loading experiments, the predicted microstructure evolutions do not present marked changes up to 1.5% of deformation. Modelling gives reasonable predictions for the evolution of the subgrain size during cycling. However, the decrement in the free dislocation density is underestimated with respect to our measured values but close to other experimental data. The predictions have been shown to be only weakly dependent on the main material parameters provided they belong to a physically-based range of variation.

Acknowledgements

The authors express their thanks to Consejo Nacional de Investigaciones Científicas y Técnicas (CONICET); to Agencia Nacional de Promoción Científica y Tecnológica (ANPCYT) of Argentina and to CEA/Direction des Relations Internationales and CEA/DISN/Réacteurs 4ème génération/Projet MASNA, France, for supporting this work. Dr Marmy is acknowledged for his fatigue tests carried out on the EUROFER 97 specimens.

Appendix A. Calculation of the geometrical factor (*l*) from Orowan's law

The geometrical factor l is given by the area enclosed by the dislocation line divided by d (distance between the LABs),

$$l = \frac{\text{area}}{d} \tag{A1}$$

Based on Fig. A1, a simple geometrical consideration leads us to link the area swept by the dislocation, the radius of curvature R, the slip length h and the angle θ by:

$$\text{area} = \theta R^2 - \frac{d}{2}(R-h) \tag{A2}$$

The θ angle is deduced from Fig. A1:

$$\theta = arctg\left(\frac{d}{2(R-h)}\right) \tag{A3}$$

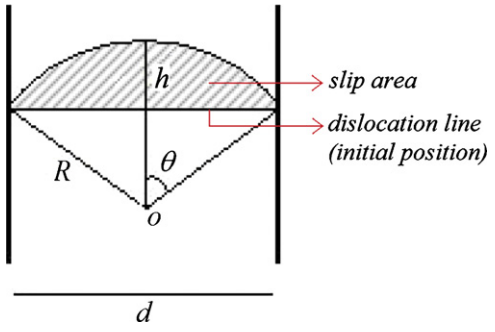

Fig. A1. Area enclosed by the dislocation (initial position and position under stress).

Considering that the slip length has to be lower than R, it is deduced from the Pythagoras' theorem:

$$h = R - \frac{1}{2}\sqrt{4R^2 - d^2} \tag{A4}$$

This allows finally the computation of the slip area using Eq. (A2),

$$l = \frac{\text{area}}{d} = \frac{1}{d}\left[R^2 arctg\left(4\frac{R^2}{d^2} - 1\right)^{-1/2} - \frac{d}{4}\left(4R^2 - d^2\right)^{1/2}\right] \tag{A5}$$

Appendix B. Back stress differential equation

Taking account of Eq. (12), the radius of curvature is expressed as follows,

$$R = \frac{\mu b}{2x^i} \tag{B1}$$

Replacing Eq. (B1) into Eq. (10),

$$\gamma^i = \frac{\left(\rho_e^i + \rho_s^i\right) b}{d}\left\{\left(\frac{\mu b}{2x^i}\right)^2 arctg\left[\left(\frac{\mu b}{dx^i}\right)^2 - 1\right]^{-1/2} - \frac{d}{4}\left[\left(\frac{\mu b}{x^i}\right)^2 - d^2\right]^{1/2}\right\} \tag{B2}$$

Assuming that mobile dislocations densities and subgrain size do not change during an infinitesimal variation in time, the time derivation of Eq. (B2) gives,

$$\dot{\gamma}^i = \frac{\left(\rho_e^i + \rho_s^i\right) b^3 \mu^2}{2d}\frac{\dot{x}^i}{\left(x^i\right)^3}\left\{\frac{1}{2}\left[\left(\frac{\mu b}{dx^i}\right)^2 - 1\right]^{-1/2} - arctg\left[\left(\frac{\mu b}{dx^i}\right)^2 - 1\right]^{-1/2}\right\} \tag{B3}$$

From Eq. (B3) it is possible to obtain $\dot{x}^i$ as a function of the shear strain rates as it is expressed in Eq. (13).

References

[1] K.L Klueh, D.R. Harries. ASTM Mono3, West Conshohocken, PA. (USA), 2001.
[2] W. Jones, C.R. Hills, D.H. Polonis, Metall. Trans. 22A (1991) 1049.
[3] A.F. Armas, C. Petersen, R. Schmitt, M. Avalos, I. Alvarez, J. Nucl. Mater. 329–333 (2004) 252.
[4] M.F. Giordana, I. Alvarez-Armas, M. Sauzay, A. Armas, Key Eng. Mater. 465 (2011) 358–361.
[5] B. Sonderegger, S. Mitsche, H. Cerjak, Mater. Charact. 58 (2007) 874–882.
[6] B. Fournier Fatigue-fluage des aciers martensitiques à 9-12%Cr: comportement et endommagement. PhD Thesis. CEA-DEN-DANS-DMN-SRMA-LC2M 91191 Gif-sur-Yvette Cedex. CEA Saclay; 2007.
[7] L. Kunz, P. Lukás, Eur. Struct. Integrity Soc. 29 (2002) 37–44.
[8] B. Fournier, M. Sauzay, A. Renault, F. Barcelo, A. Pineau, J. Nucl. Mater. 386–388 (2009) 71–74.
[9] B. Fournier, M. Sauzay, A. Pineau, Int. J. Plast. 27 (2011) 1803–1816.
[10] P.J. Ennis, A. Zielinska-Lipiec, O. Wachter, A. Czyrska-Filemonowicz, Acta Mater. 45 (1997) 4901–4907.
[11] P.F. Giroux, F. Dalle, M. Sauzay, C. Caës, B. Fournier, T. Morgeneyer, A.F. Gourgues-Lorenzon, Proc. Eng. 2 (2010) 2141.
[12] P.F. Giroux, F. Dalle, M. Sauzay, J. Malaplate, B. Fournier, A.F. Gourgues-Lorenzon, Mater. Sci. Eng. A 527 (2010) 3984–3993.
[13] A.F. Armas, M. Avalos, I. Alvarez-Armas, C. Petersen, R. Schmitt, J. Nucl. Mater. 258–263 (1998) 1204–1208.
[14] P. Marmy, T. Kruml, J. Nucl. Mater. 377 (2008) 52–58.
[15] P. Marmy, J. Nucl. Mater. 367–370 (2007) 86–91.
[16] B. Fournier, F. Dalle, M. Sauzay, J. Longour, M. Salvi, C. Caës, et al., Mater. Sci. Eng. A 528 (2011) 6934–6945.
[17] Suresh, Fatigue of Materials, 2nd edition, Cambridge University Press, Cambridge, 1998.
[18] B. Fournier, M. Sauzay, C. Caës, M. Noblecourt, M. Mottot, Mater. Sci. Eng. A 437 (2006) 183–196.
[19] T. Kruml, J. Polák, J. Nucl. Mater. 412 (2011) 2–6.

[20] B. Fournier, M. Salvi, F. Dalle, Y. De Carlan, C. Caës, M. Sauzay, A. Pineau, Int. J. Fatigue 32 (2010) 971–978.
[21] S. Dubey, H. Chilukuru, J.K. Chakravartty, M. Schwienheer, A. Scholz, W. Blum, Mater. Sci. Eng. A 406 (2005) 152–159.
[22] C. Vorpahl, A. Möslang, M. Rieth, J. Nucl. Mater. 417 (2011) 16–19.
[23] E. Kröner, Acta Metall. 9 (1961) 155.
[24] J.M. Marder, A.R. Marder, Trans. ASME 62 (1969) 1.
[25] H. Kitahara, R. Ueji, N. Tsuji, Y. Minamino, Acta Mater. 54 (2006) 1279–1288.
[26] H. Klaar, P. Schwaab, W. Österle, Prakt. Metallogr. 29 (1992) 3.
[27] G. Thomas, Transmission Electron Microscopy of Metals, John Wiley & Sons Inc., New York, 1964.
[28] J. Pešička, R. Kužel, A. Dronhofer, G. Eggeler, Acta Mater. 51 (2003) 4847–4862.
[29] J.R. Taylor, An introduction to Error Analysis: The Study of Uncertainties in Physical Measurements, 2nd edition, University Science Book, 1997.
[30] S. Kim, J.R. Weertman, Metall. Trans. 19A (1988) 999.
[31] R. Kannan, R. Sandhya, V. Ganesan, M. Valsan, K. Bhanu Sankara Rao, J. Nucl. Mater. 384 (2009) 286–291.
[32] L. Kunz, P. Lukáš, Eur. Struct. Integrity Soc. 29 (2000) 37–44.
[33] R.W.K. Honeycombe, Steels: Microstructure and Properties, 1st ed., Edward Arnold (Publishers), London, 1981, pp. 12–13.
[34] F. Rachdi, M. Sauzay, Congres Francais de Mecanique. Besancon, France, Sept 2011.
[35] S. Naamane Etude de la deformation plastique de la ferrite a basse temperature: simulations de dynamique des dislocation. PhD Thesis. Universite Pierre et Marie Curie; 2008.
[36] C. Sommer, H. Mughrabi, D. Lochner, Acta Mater. 46 (5) (1998) 1527.
[37] D. Caillard, J.L. Martin, Thermally Activated Mechanisms in Crystal Plasticity, vol. 8, Pergamon, 2003.
[38] U. Essmann, H. Mughrabi, Philos. Mag. 40 (1979) 731.
[39] M. Sauzay, Mater. Sci. Eng. A 510–511 (2009) 74–80.
[40] D. Holec, A. Dlouhy, Z. Metallkd. 96 (2005) 558–565.
[41] K. Wakasa, C.M. Wayman, Acta Metall. 29 (1981) 991–1011.
[42] L. Guétaz, J.P., Millier, S. Urvoy Mécanisme de déformation de l'acier martensitic Eurofer. Note technique CEA/DTEN/SMP/LSMM 2002-128. 2003.
[43] U. Essmann, K. Differt, Mater. Sci. Eng. A 208 (1996) 56–68.
[44] L. Brown, Philos. Mag. 86 (2006) 4055.
[45] J. El-Awady, N. Ghoniem, H. Mughrabi, Proc. of the 136th TMS Annual Meeting and Exhibition, Florida, 2007, pp. 23–35.
[46] D. Hull, Introduction to Dislocations, Pergamon Press, 1965, p. 80.
[47] L. Dupuy, M.C. Fivel, Acta Mater. 50 (2002) 4873–4885, Materials Series; 2003.
[48] L. Guetaz, Y. de Carlan, F., Barcelo, J.P., Millier, S., Urvoy, P. Widen t, Mécanismes de déformation de l'acier martensitique EUROFER. CEA Report, Note Technique DTEN N°2002/20, 2002.
[49] Y. de Carlan, L. Guetaz Analyse morphologique et cristallographique de la structure martensitique dans l'acier EUROFER. Note Technique CEA/DEN/DMN/SRMA 00-2400, 2000.
[50] L. Kunz, P. Lukáš, Mater. Sci. Eng. A 319–321 (2001) 555–558.
[51] R. Hill, J. Mech. Phys. Solids 13 (1965) 89.
[52] J.W. Hutchinson, J. Mech. Phys. Solids 319 (1970) 247.
[53] A. Molinari, S. Ahzi, R. Kouddane, Mech. Mater. 26 (1997) 43–62.